Sustainable Energy & Fuels

ROYAL SOCIETY OF CHEMISTRY

PAPER

View Article Online
View Journal | View Issue

Check for updates

Cite this: *Sustainable Energy Fuels*, 2025, **9**, 6761

Process modelling and thermodynamic analysis of hydrogen production through chemical looping ammonia cracking

Anantha Krishnan Vinayak Soman, Siqi Wang, * Ziqi Shen and Mingming Zhu

Received 23rd July 2025
Accepted 22nd October 2025

DOI: 10.1039/d5se01010a

rsc.li/sustainable-energy

In this study, a novel chemical looping ammonia cracking (CLCr) process was designed for efficient hydrogen production. A closed-loop, three-reactor chemical looping system using iron oxide as the oxygen carrier was modelled in Aspen Plus. A parametric study was carried out to evaluate the effect of key parameters, including the air reactor outlet temperature, fuel reactor outlet temperature, ammonia to oxygen carrier ratio, and the steam reactor pressure. The optimal operating conditions were then identified, under which a hydrogen yield of 69.4% with 99.99% purity can be achieved with an overall energy efficiency of 79.6%. An energy balance analysis was also carried out to confirm that the process is autothermal, and the overall exergy efficiency of the process was 70.4%. These findings highlight the novel CLCr process as an energy-efficient alternative to conventional ammonia catalytic cracking for hydrogen production.

Open Access Article. Published on 31 2025. Downloaded on 14.12.2025 04:25:05.
This article is licensed under a Creative Commons Attribution 3.0 Unported Licence.

Introduction

Hydrogen has gained increasing attention as a clean energy vector in the transition to a net-zero future. Different sustainable hydrogen production pathways are being developed to complement conventional fossil fuel-based processes, such as water electrolysis and biomass gasification.[1] However, a common challenge across all pathways is the need for safe, efficient, and scalable storage and distribution of hydrogen. As a mature commodity, ammonia has emerged as a promising hydrogen carrier, due to its high hydrogen content (17.8 wt%), easy storage, and well-established global infrastructure network for production, distribution, and storage, developed over a century of large-scale use in the fertiliser industry.[2–4]

As a hydrogen carrier, ammonia needs to be converted back to hydrogen at the end-use point. Currently, the predominant pathway to convert ammonia into hydrogen is through thermocatalytic ammonia cracking. One of the limitations of this process is that the reaction is highly endothermic (46 kJ mol^{-1} NH_3) with additional energy required for liquid ammonia vaporisation (23.4 kJ mol^{-1}) and preheating (liquid ammonia heat capacity of 50 J mol^{-1} K^{-1}).[5] Moreover, of all the catalysts tested for the reaction, Ru-based catalysts remain the performance benchmark, limiting the scalability of the process due to their cost. Although non-noble metal-based and bimetallic alternatives have been studied, the reaction temperature required for these catalysts to reach a desirable reaction rate remains high.[6,7] Aside from the kinetics and catalyst limitations, an inherent challenge of the process is the extensive purification process required for the reactor off-gas, which contains a 1 : 3 molar ratio mixture of N_2 to H_2 with unreacted NH_3, to produce a high-purity hydrogen stream.

The Chemical Looping (CL) technology provides a suitable option to address the challenges faced by conventional thermocatalytic ammonia cracking. CL has been extensively studied for hydrogen production from methane and other hydrocarbon fuels.[8–12] In addition, the CL process can be integrated with renewable energy and bio-feedstocks to improve energy efficiency and reduce carbon emission. For example, solar-assisted chemical looping systems have been proposed to combine redox cycles with concentrated solar energy, significantly improving hydrogen yield while reducing emissions.[13] CO_2-rich waste gases, such as landfill gases, have also been explored as alternative feedstocks for syngas production, offering a sustainable route for both hydrogen production and CO_2 utilisation.[14]

A typical three-reactor CL process involves three main steps: (1) the reactions between the fuel and the oxygen carrier (metal oxides) to produce carbon dioxide in the Fuel Reactor (FR); (2) the reactions between the reduced oxygen carrier and steam to produce hydrogen in the Steam Reactor (SR); (3) the reaction between the oxygen carrier and air to regenerate the oxygen carrier and produce an oxygen-depleted N_2 stream in the Air Reactor (AR).

In this study, a closed-looped three-reactor CL process for ammonia cracking is conceptualised, named as Chemical Looping Ammonia Cracking (CLCr), where iron oxide is used as the oxygen carrier to crack ammonia and produce ultra-high purity hydrogen. Iron oxide was selected as the oxygen carrier

Faculty of Engineering and Applied Sciences, Cranfield University, Bedford, MK43 0AL, United Kingdom. E-mail: siqi.wang2019@cranfield.ac.uk

Open Access Article. Published on 31 2025. Downloaded on 14.12.2025 04:25:05. This article is licensed under a Creative Commons Attribution 3.0 Unported Licence.

(OC) due to its abundance, thermal stability, and low cost.[15] In the chemical looping reforming (CLR) process, iron oxides also showed good reactivity, high oxygen adsorption capacity, and high resistance against sintering.[16,17] Recent studies on iron ore direct reduction using ammonia suggest that it is feasible to use iron oxides as an oxygen carrier for ammonia reduction.[18,19] Furthermore, experimental thermogravimetric analyses reported by Ma *et al.* showed that Fe_2O_3 can be fully reduced under NH_3 at 700 °C without the formation of NO_x,[20] confirming its reducibility under ammonia-rich environment. In addition, metallic Fe – formed upon complete reduction of iron oxides – has been demonstrated to be active for ammonia decomposition.[21] These experimental findings are consistent with the reaction pathways considered in this work, providing confidence in the feasibility of the proposed process. This work aims to design a CLCr process *via* Aspen Plus modelling and evaluate the effect of key process parameters on the performance of the system through a parametric analysis. Finally, a process was developed using the optimal operation conditions identified in the parametric analysis and the thermodynamic analysis was carried out on the optimised process.

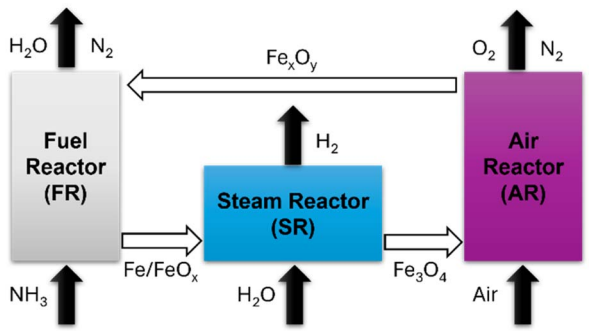

Fig. 1 Block diagram of the proposed ammonia CLCr process.

Methodology

Process description

The novel CLCr process proposed in this work consists of three main reactors, the fuel reactor (FR), the steam reactor (SR), and the air reactor (AR). A block diagram of the process is shown in Fig. 1. The reactions which take place in the three reactors are summarised in Table 1.

Aspen Plus model setup

The steady-state modelling of the proposed CLCr process was carried out using the Aspen Plus v12.2 software. The components used in the model are summarised in Table 2. N_2O and NO were defined as components to estimate NO_x formation in the FR. Fe_4N was included as a component, as its formation from the reaction between Fe^0 and ammonia hinders the reoxidation of Fe^0.[18] Considering the potential sintering and attrition of the OC material under real-life conditions, Al_2O_3 was

Table 2 List of components used in the Aspen Plus model

Name	Type	Component name	Databank
Fe_2O_3	Solid	Hematite	APV121.PU
Fe_3O_4	Solid	Magnetite	APV121.SOLIDS
$Fe_{0.947}O$	Solid	Wustite	APV121.INORGANIC
Fe	Solid	Iron	APV121.PURE39
Al_2O_3	Solid	Alumina	APV121.PURE39
Fe_4N	Solid	Iron nitride	APV121.INORGANIC
NH_3	Conventional	Ammonia	APV121.PURE39
N_2	Conventional	Nitrogen	APV121.PURE39
H_2	Conventional	Hydrogen	APV121.PURE39
O_2	Conventional	Oxygen	APV121.PURE39
H_2O	Conventional	Water	APV121.PURE39
NO_2	Conventional	Nitrogen dioxide	APV121.PURE39
NO	Conventional	Nitric oxide	APV121.PURE39
N_2O	Conventional	Nitrous oxide	APV121.PURE39

Table 1 List of reactions which take place in the CLCr process

Fuel reactor	$NH_3 \xrightarrow{Fe/Fe_3O_4} 0.5N_2 + 1.5H_2,\ \Delta H^\circ_{298} = +45.94\text{kJ mol}^{-1}$ (1)
	$Fe_2O_3 + 0.222NH_3 \rightarrow 0.667Fe_3O_4 + 0.111N_2 + 0.333H_2O,\ \Delta H^\circ_{298} = +7.28\text{kJ mol}^{-1}$ (2)
	$Fe_3O_4 + 0.554NH_3 \rightarrow 3.168Fe_{0.947}O + 0.277N_2 + 0.832H_2O,\ \Delta H^\circ_{298} = +83.30\text{kJ mol}^{-1}$ (3)
	$Fe_{0.947}O + 0.667NH_3 \rightarrow 0.947Fe + 0.333N_2 + H_2O,\ \Delta H^\circ_{298} = +76.15\text{kJ mol}^{-1}$ (4)
	$Fe_2O_3 + 0.333H_2 \rightarrow 0.667Fe_3O_4 + 0.333H_2O\ ,\ \Delta H^\circ_{298} = -2.66\text{kJ mol}^{-1}$ (5)
	$Fe_3O_4 + 0.832H_2 \rightarrow 3.168Fe_{0.947}O + 0.832H_2O,\ \Delta H^\circ_{298} = +57.86\text{kJ mol}^{-1}$ (6)
	$Fe_{0.947}O\ +\ H_2 \rightarrow 0.947Fe + H_2O,\ \Delta H^\circ_{298} = +30.21\text{kJ mol}^{-1}$ (7)
	$Fe_3O_4 + 0.788Fe \rightarrow 4Fe_{0.947}O + H_2O,\ \Delta H^\circ_{298} = +32.73\text{kJ mol}^{-1}$ (8)
	$Fe_{0.947}O \rightarrow 0.25Fe_3O_4 + 0.197Fe,\ \Delta H^\circ_{298} = -8.18\text{kJ mol}^{-1}$ (9)
Steam reactor	$Fe + 1.056H_2O(g) \rightarrow Fe_{0.947}O\ + 1.056H_2,\ \Delta H^\circ_{298} = -31.90\text{kJ mol}^{-1}$ (10)
	$Fe + 1.056H_2O(l) \rightarrow Fe_{0.947}O + 1.056H_2,\ \Delta H^\circ_{298} = +14.56\text{kJ mol}^{-1}$ (11)
	$Fe_{0.947}O + 0.263H_2O(g) \rightarrow 0.316Fe_3O_4 + 0.263H_2,\ \Delta H^\circ_{298} = -18.56\text{kJ mol}^{-1}$ (12)
	$Fe_{0.947}O + 0.263H_2O(l) \rightarrow 0.316Fe_3O_4 + 0.263H_2, \Delta H^\circ_{298} = -6.98\text{kJ mol}^{-1}$ (13)
	$Fe + 1.333H_2O(g) \rightarrow 0.333Fe_3O_4 + 1.333H_2,\ \Delta H^\circ_{298} = -48.26\text{kJ mol}^{-1}$ (14)
	$Fe + 1.333H_2O(l) \rightarrow 0.333Fe_3O_4 + 1.333H_2,\ \Delta H^\circ_{298} = +10.26\text{kJ mol}^{-1}$ (15)
Air reactor	$Fe_{0.947}O + 0.211O_2 \rightarrow 0.474Fe_2O_3,\ \Delta H^\circ_{298} = -119.00\text{kJ mol}^{-1}$ (16)
	$Fe_3O_4\ + 0.25O_2 \rightarrow 1.5Fe_2O_3,\ \Delta H^\circ_{298} = -117.36\text{kJ mol}^{-1}$ (17)

 This journal is © The Royal Society of Chemistry 2025

Open Access Article. Published on 31 2025. Downloaded on 14.12.2025 04:25:05.
This article is licensed under a Creative Commons Attribution 3.0 Unported Licence.

Table 3 Properties used for the main blocks and model assumptions

Subjects	Selection	References
Properties		
Property method	PR-BM	28–31
Steam class	MIXCISLD	32
Unit operation blocks		
Reactors	RGibbs	30, 31, 33 and 34
Heat exchangers	HeatX	35
Heaters	Heater	28
Pressure changers	Compr, valve	28
Separators	Flash2	28
Assumptions		
Ambient conditions	1 atm, 25 °C	34
Pressure drops	Zero	30, 33 and 36–38
Air	79 mol% N_2, 21 mol% O_2	28, 34 and 39
Minimum approach temperature (MAT) of heat exchangers	10 °C	34, 40 and 41
Minimum approach temperature (MAT) of steam generator	10 °C	34, 40 and 41
Minimum approach temperature (MAT) of ammonia vaporiser	3 °C	41
Isentropic efficiency-compressor	89%	34 and 42
Mechanical efficiency-compressor	97%	34 and 40
Pump efficiency	90%	34 and 40
Isentropic efficiency-turbine	93%	34 and 42
Mechanical efficiency-turbine	96.6%	40 and 42
Generator efficiency	99%	43
Reactors of FR, AR and SR	Adiabatic, Gibbs free energy minimisation	40
Reactor operating pressure	1 atm	29 and 38
Feed ammonia stream conditions	10 bar, 25 °C	44
Cooling utility (air/water)	25 °C	

included as a heat carrier with Fe_2O_3 for its good specific heat capacity.[22,23] Al_2O_3 was regarded as an inert material, thus the $FeAl_2O_4$, formed by the reaction between Fe_2O_3 and Al_2O_3, was not defined as a component.[24–26] RGibbs blocks were used to simulate all reactors, accounting for all possible reaction pathways within the defined components and neglecting mass transfer limitations.[26] The counter-current moving-bed reactor was selected for the FR, which was simulated by 7 RGibbs blocks. The SR and AR were simulated by one RGibbs block each. The counter-current moving-bed reactors, based on the experimental and modelling study of a 25 kW_{th} syngas CL system using iron-based OCs, achieved high syngas conversion and continuous production of high-purity hydrogen.[27] The system was simulated under a pressure of 1 bar, and its performance was assessed across an AR outlet temperature (T_{Ao}) in the range of 880 – 1150 °C. The properties of the main blocks and the assumptions made for the model development are summarised in Table 3.

System performance evaluation

To evaluate the performance of the process, 8 metrics were used with their definitions and equations summarised in Table 4.

The thermodynamic analysis also includes heat balance, which can be evaluated using the following method. Under autothermal conditions, the net heat of oxidation of the steam in the SR (ΔH^0_{SR}) plus the heat of combustion of hydrogen should be equal to the heat of oxidation of the equivalent OC in AR (ΔH^0_{AR}), defined as below:

$$\Delta H^R_{Red} + \Delta H^0_{Comb_{H_2}} + \Delta H^0_{AR} + \Delta H^0_{SR} = \Delta H^0_{Comb_{NH_3}} \quad (29)$$

In the meantime:

$$\Delta H^R_{Red} = \left|\Delta H^0_{Comb_{NH_3\text{-fuel}}}\right| + \left|\Delta H^0_{SR}\right| \quad (30)$$

where $\Delta H^0_{Comb_{NH_3\text{-fuel}}}$ is the fuel fraction of ammonia in the ammonia CLCr process. Fig. 2 shows the energy inputs and outputs in the CLCr process. For the calculation of the heat consumed in FR ($Q_{heat\text{-}sink}$), the following were considered: the heat from input oxides (Q_i) and gas (Q_{NH_3}), the heat remaining in the output reduced oxides (Q_o), and direct loss (Q_v).

The heat input can be calculated with eqn (31) and (32):

$$Q_i = m_i C_{pi}(T_{Ao} - 25) \quad (31)$$

$$Q_{NH_3} = M_{NH_3} C_{p\text{–}NH_3}(T_{NH_3} - 25) \quad (32)$$

The heat remaining in the output reduced oxides can be calculated with eqn (33):

$$Q_o = m_o C_{po}(T_{Fo} - 25) \quad (33)$$

Open Access Article. Published on 31 2025. Downloaded on 14.12.2025 04:25:05. This article is licensed under a Creative Commons Attribution 3.0 Unported Licence.

Table 4 8 Performance evaluation metrics in this study

Metrics	Definitions
Hydrogen yield	$Y_{H_2}(\%) = \frac{M_{H_2}}{M_{NH_3} \times 0.178} \times 100$ (18) In which M_{H_2} and M_{NH_3} were the mass flow rates of hydrogen and ammonia in kg h^{-1}, respectively
Overall energy efficiency based on lower heating value (LHV)	$\eta_{OEE} = \frac{LHV_{H_2}M_{H_2}}{LHV_{NH_3}M_{NH_3} + \frac{W_{comp}}{\eta_{heat\ to\ power}} + \frac{Q_{process}}{\eta_{comp}}}$ (19) In which LHV_{H_2}, LHV_{NH_3} were the lower heating value of hydorgen ad ammonia in kJ kg^{-1}, respectively. W_{comp} was the power requirement for compression in kWh. $Q_{process}$ was the external heat requirement of the process. The conversion efficiency from heat to power $\eta_{heat\ to\ power} = 0.123$ kWh MJ^{-1}. The efficiency $\eta_{comp} = 0.89$
Cold gas efficiency based on higher heating value (HHV)	$\eta_{CGE} = \frac{HHV_{H_2}M_{H_2}}{HHV_{NH_3}M_{NH_3}}$ (20) In which HHV_{H_2}, HHV_{NH_3} were the higher heating value of hydrogen ad ammonia in kJ kg^{-1}, respectively
Extent of reduction	$E_{red} = \frac{M_{Fe_2O_3} - M_{RedOx}}{M_{Fe_2O_3} - M_{Fe}}$ (21) In which M_{Fe_2O3}, M_{RedOx}, and M_{Fe} were the mass flow rates of iron oxide (Fe_2O_3), reduced oxides of iron, and fully reduced iron oxides (Fe), respectively
Theoretical maximum hydrogen generation	$\dot{m}_{H_2,max}\left(\frac{kg}{h}\right) = 2 \times MW_{H_2} \times (F_{O_2} - F_{O_2}^{Fe_3O_4})$ (22) $F_{O_2}^{Fe_3O_4} = \frac{\left[M_{Fe_2O_3} - 0.667 \times \left(\frac{M_{Fe_2O_3}}{MW_{Fe_2O_3}}\right) \times MW_{Fe_3O_4}\right]}{MW_{O_2}}$ (23) In which M_{Fe_2O3} was the mass flow rate of Fe_2O_3 in kg h^{-1}. MW_{O_2}, MW_{H_2}, $MW_{Fe_2O_3}$, $MW_{Fe_3O_4}$ were the molar mass of O_2, H_2, Fe_2O_3 and Fe_3O_4 in kg $kmol^{-1}$. F_{O_2} and $F_{O_2}^{Fe_3O_4}$ were the molar flow rates of O_2 and the O_2 consumed by the reaction with Fe_3O_4
Theoretical maximum hydrogen yield	$Y_{Theo} = \frac{\dot{m}_{H_2,max}}{0.178 \times M_{NH_3}}$ (24)
Fraction of fuel energy loss	$F_L = \frac{Q_{Loss}}{M_{NH_3}HHV_{NH_3}} \times 100$ (25) In which Q_{Loss} was the total process heat loss in kJ h^{-1}
Exergy efficiency of the process	$\eta_e = \frac{Ex_{H_2}}{Ex_{feed} + \frac{W_{comp}}{\eta_{heat\ to\ power}}}$ (26) In which Ex_{H_2} and Ex_{feed} were the total exergy of hydrogen and the feed gas, respectively. Two types of exergies were considered, the chemical and the physical exergy. The total exergy was defined as the sum of the two types of exergies $Ex_{total} = Ex_{chemical} + Ex_{physical}$ (27) The chemical exergy of the gas mixture can be calculated using the equation below $Ex_{chemical} = N_i\left[\sum_{i=1}^{n} Ex_i + RT_0 x_i \sum_{i=1}^{n} x_i \ln x_i\right]$ (28) In which N_i and x_i were the number of moles and the mole fraction of the component i in the gas mixture, respectively

The heat loss in FR vent (Q_v) can be collected from the model.

The net heat consumed in FR can be then calculated using eqn (34):

$$Q_{heat\text{-}sink} = Q_i + Q_{NH_3} - Q_o - Q_v \quad (34)$$

For the calculation of the net heat generated in heat source ($Q_{heat\text{-}source}$), the following were considered: the heat from the fuel-fraction of ammonia ($\Delta H^0_{Comb_{NH_3\text{-}fuel}}$), the heat of oxidation of the steam in the SR (ΔH^0_{SR}). The heat loss from the AR and SR vent were considered as 0 as the AR gas vent was cooled to 25 °C and the SR gas vent was cooled to be below zero in the model.

The fuel-fraction of the mass flow of ammonia ($M_{NH_3\text{-}fuel}$) can be calculated using eqn (35):

$$M_{NH_3-fuel} = M_{NH_3} - \frac{M_{H_2}}{0.178} \quad (35)$$

The heat of oxidation of the steam in the SR (ΔH^0_{SR}) can be collected from the model.

$$\Delta H^0_{Comb_{NH_3\text{-}fuel}} = HHV \cdot M_{NH_3\text{-}fuel} \quad (36)$$

The net heat generated in the SR and AR can then be calculated using (eqn (37)):

$$Q_{heat\text{-}source} = \Delta H^0_{Comb_{NH_3\text{-}fuel}} + \Delta H^0_{SR} \quad (37)$$

 This journal is © The Royal Society of Chemistry 2025

Open Access Article. Published on 31 2025. Downloaded on 14.12.2025 04:25:05.
This article is licensed under a Creative Commons Attribution 3.0 Unported Licence.

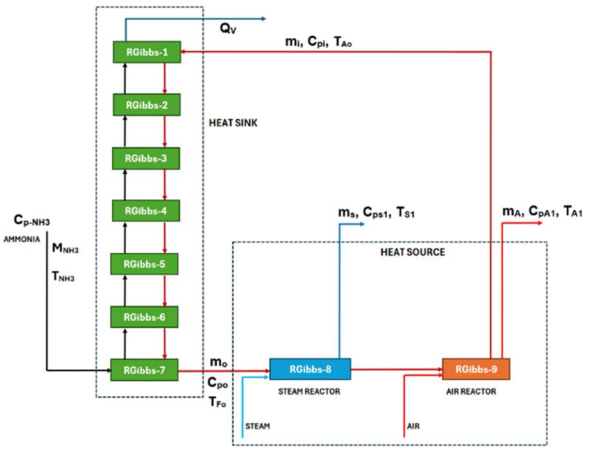

Fig. 2 Schematic diagram of the heat flow of the CLCr process. Q_v: the vent heat loss from the FR in MJ h^{-1}. M_{NH_3}: the total flow rate of ammonia in kg h^{-1}. m_k ($k = s, A, i, o$): the mass flow rates of the SR vent, AR vent, FR inlet solid, and FR solid in kg h^{-1}. C_{pk} ($k = s1, A1, NH_3, o, i$): the mass-specific heat capacities of the SR vent, AR vent, ammonia, FR outlet solid, and FR inlet solid in kJ kg^{-1} $°C^{-1}$. T_k ($k = Ao, S1, A1, NH_3, Fo$): temperatures of the FR inlet, SR outlet gas after cooling, AR vent after heat recovery, ammonia inlet, and the FR outlet.

Results and discussion

Parametric study

Based on the block program (Fig. 1), an Aspen Plus model was developed, and an example of the schematic diagram is presented in Fig. 3. Four key parameters were chosen to evaluate their effects on the model performance: the AR outlet temperature (T_{Ao}), the FR outlet temperature (T_{Fo}), the ammonia to oxygen carrier ratio ($R_{NH_3/OC}$, based on mass flow rates), and the SR pressure.

Effect of the AR outlet temperature (T_{Ao})

In this section, the effect of T_{Ao} within the range of 880 – 1080 °C was evaluated, and the results are presented in Fig. 4. Temperatures below 880 °C were excluded to ensure high levels of OC reduction and to prevent $Fe_{0.947}O$ disproportionation in the FR. In this study, the solid at the AR outlet remained fully oxidised at stoichiometric air conditions with a circulation rate of 20 000 kg h^{-1}. The Fe_2O_3 mass fraction was 0.758, with the remainder being the heat carrier, Al_2O_3. The flow rate of ammonia was fixed at around 1400 kg h^{-1}, simulating the scale

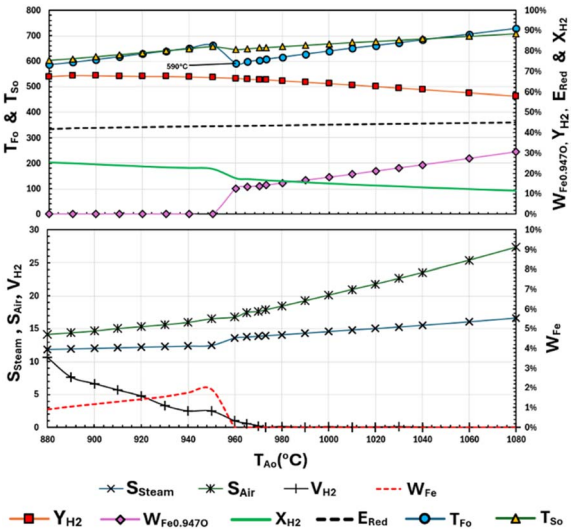

Fig. 4 Effect of T_{Ao} on hydrogen yield (Y_{H_2}), extent of reduction (E_{red}), mass fractions of $Fe_{0.947}O$ and Fe slip to AR ($W_{Fe_{0.947}O}$, W_{Fe}), specific steam consumption (S_{steam}), specific air consumption (S_{air}), mass fractions of H2 in the SR gas outlet (X_{H_2}) and H2 in the FR vent (V_{H_2}), SR outlet temperature (T_{So}), and FR outlet temperature (T_{Fo}).

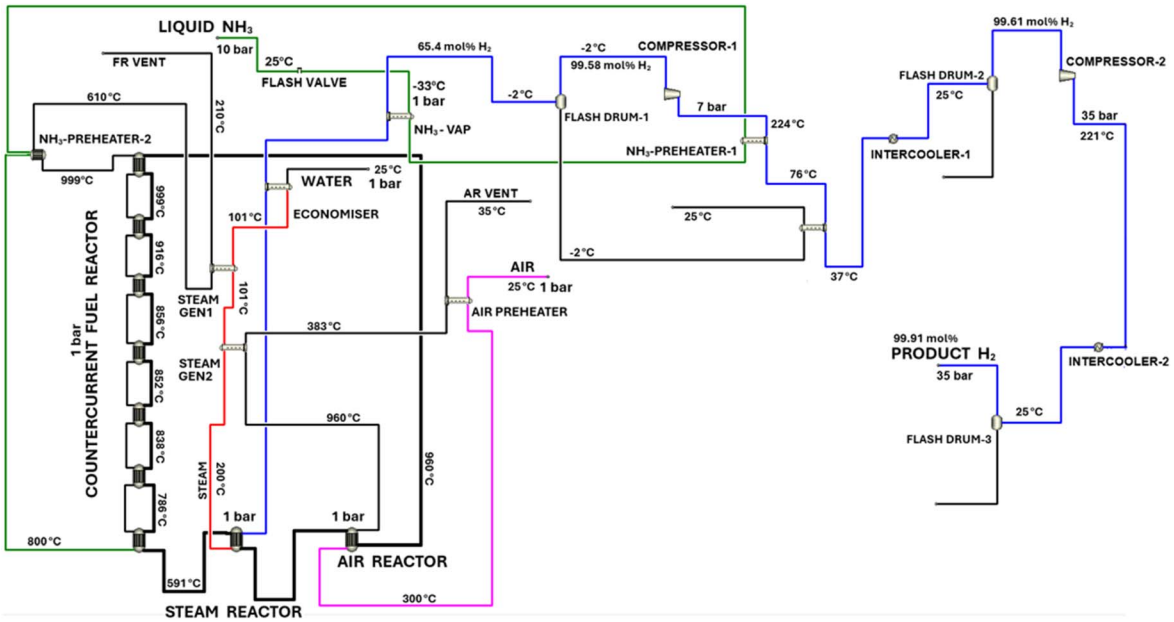

Fig. 3 Schematic diagram of the Aspen Plus model with $T_{Ao} = 960$ °C.

Open Access Article. Published on 31 2025. Downloaded on 14.12.2025 04:25:05.
This article is licensed under a Creative Commons Attribution 3.0 Unported Licence.

of H_2 production of approximately 200 kg h^{-1}, capacity suitable for applications in hydrogen refuelling stations or for on-site fuel cells.

As T_{Ao} increases, E_{red} increases due to thermodynamic favourability.[45] Y_{H_2} increases when T_{Ao} increases from 880 °C to 890 °C, however, it stablises and decreases when T_{Ao} increases further from 960 °C. It can be observed that T_{Fo} and T_{So} increase with T_{Ao}, but there is a significant decrease when T_{Ao} is around 960 °C. Meanwhile, $W_{Fe_{0.947}O}$ suddenly increases from zero when T_{Ao} rises above 960 °C, while W_{Fe} drops to zero. When T_{Ao} is at 960 °C, T_{Fo} is about 590 °C, which corresponds to the disproportionation temperature of iron oxide. The phase diagram of iron oxides with the presence of steam shows that the Wustite phase ($Fe_{0.947}O$) appears when the SR temperature is above the disproportionation temperature.[46] Below this temperature, Fe can be directly oxidised to Fe_3O_4, so the fuel reactor (FR) and the steam reactor (SR) are in the Fe ↔ Fe_3O_4 phase equilibria. This explains the sudden increase in $W_{Fe0.947O}$ as the equilibria shifts from Fe ↔ Fe_3O_4 to Fe ↔ $Fe_{0.947}O$ ↔ Fe_3O_4 when T_{Ao} exceeds 960 °C.

H_2 in the FR vent (V_{H_2}) decreases as T_{Ao} increases up to 960 °C and then remains almost zero when the T_{Ao} is greater than 960 °C, meaning that no hydrogen is produced in the FR. This may be due to the increase in the reduction rate in the FR until the peak value at 590 °C (T_{Fo}). In terms of E_{red}, about 11% (calculation is shown in SI) of Fe_2O_3 in the FR is unutilised due to the thermodynamic barrier in re-oxidation in the SR.[47] In other words, only 89% Fe_2O_3 contributes to the production of Y_{H_2} in the process. When T_{Ao} increases from 880 to 960 °C, W_{Fe} increases, and more Fe converts to Fe_3O_4 in the SR. This explains why Y_{H_2} remains stable when E_{red} increases. However, the conversion between $Fe_{0.947}O$ and Fe_3O_4 in the SR results in a lower Y_{H_2} when T_{Ao} is above 960 °C.

On the other hand, S_{steam} and S_{air} increase as T_{Ao} increases, while X_{H_2} decreases. The increase in S_{steam} with T_{Ao} is due to the rise in T_{Fo}. With a constant total ammonia feed rate (M_{NH_3}), the endothermic heat requirement remains unchanged, which causes excess heat carry-over in the reduced iron oxides to the SR. A higher T_{Fo} results in a lower steam equilibrium conversion, indicating that more steam is needed to sustain the oxidation of the reduced iron oxides.[39] Due to an increased S_{steam}, X_{H_2} decreases as T_{Ao} rises. The NH_3 CLCr process conceptualised in this work consists of an energy-intensive steam production step, which consumes 50–60% of all recovered heat. Additionally, the high steam mass fraction in the SR outlet ($1 - X_{H_2}$) raises the latent heat load, limiting the extent of gas cooling and condensation in the ammonia vaporiser. This results in more compression work in the purification section, due to higher average gas molar mass resulting from higher moisture content in the gas exiting the vaporiser. The step changes can be observed when T_{Ao} is around 960 °C for all the three parameters mentioned above. As mentioned previously, the equilibria shift from Fe ↔ Fe_3O_4 to Fe ↔ $Fe_{0.947}O$ ↔ Fe_3O_4 leads to significant increases the P_{H_2O}/P_{H_2} requirement in the SR, which in turn results in a higher steam consumption and lower X_{H_2}. When T_{Ao} is lower than 960 °C, S_{air} increases as more W_{Fe} requirement in the AR. When T_{Ao} is higher than 960 °C, S_{air} increases as more $Fe_{0.947}O$ is required to enable a higher reaction temperature in the AR, which compromises the conversion of Fe_3O_4 to $Fe_{0.947}O$ in the SR.

Effect of FR outlet temperature (T_{Fo})

In this section, the inlet oxide feed for the converged model (Fig. 3) when T_{Ao} is 960 °C was applied ($Fe_{0.947}O$ 61.58%, Fe 11.56%, balanced by Al_2O_3). With an M_{NH_3} of 1380 kg h^{-1}, the maximum hydrogen generation ($\dot{m}H_2$, max) is 186.9 kg h^{-1} (calculation shown in Supplementary Information). The effect of T_{Fo} within the range of 150–900 °C was evaluated. In addition to T_{Fo}, the steam flow between 1000 and 4000 kg h^{-1} was also considered.

The results are presented in the form of a mesh plot, showing the flow rate of hydrogen (M_{H_2}) at various T_{Fo} and steam flow (Fig. 5). The six areas highlighted by the dashed lines represent different states of equilibria inside the SR. Area 6 shows the steam flow rate at different T_{Fo} to reach the maximum hydrogen generation ($\dot{m}H_2$, max = 186.9 kg h^{-1}). When M_{H_2} is constant (the horizontal lines shown in Fig. 5), more steam is consumed as T_{Fo} increases. The specific steam consumption (S_{steam}) increases as steam is consumed faster at higher T_{Fo}. Area 1 illustrates the scenario with low S_{steam}. At this stage, the system in the SR is in the Fe ↔ Fe_3O_4 phase equilibria, where lower P_{H_2O}/P_{H_2} is required for the conversion.[46] This scenario (high M_{H_2} achieved at low T_{Fo}) seems advantageous, but Collins-Martinez *et al.* advised a minimum T_{Fo} of 400 °C in the SR to avoid slow kinetics.[39] When T_{Fo} is higher than the

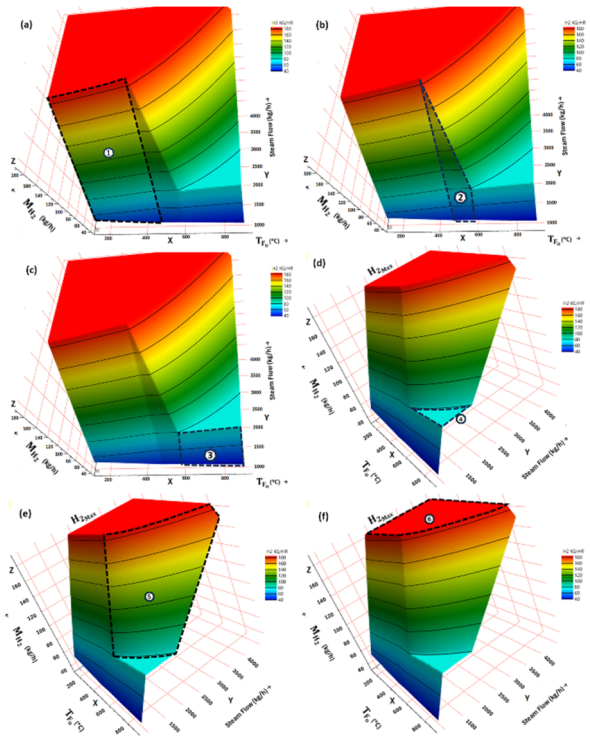

Fig. 5 Mesh plots of hydrogen production (M_{H_2}) as a function of fuel reactor outlet temperature (T_{Fo}) and steam flow at T_{Ao} = 960 °C, with six highlighted areas.

This journal is © The Royal Society of Chemistry 2025

Open Access Article. Published on 31 2025. Downloaded on 14.12.2025 04:25:05. This article is licensed under a Creative Commons Attribution 3.0 Unported Licence.

disproportionation temperature (~590 °C), a stable hydrogen flowrate (80.6 kg h^{-1}) can be observed at low steam flowrate (area 4) (calculation shown in Supplementary Information). As the specific steam flow rate (S_{steam}) increases, the hydrogen flow rate increases significantly (area 5). At low S_{steam}, the hydrogen is generated from Fe-phase only (area 3). Hydrogen generated solely from the Fe-phase reaches its maximum (80.6 kg.h^{-1}) at area 4. By increasing S_{steam}, and there by P_{H_2O}/P_{H_2}, the equilibria shifts from Fe ↔ Fe_3O_4 to Fe ↔ $Fe_{0.947}O$ ↔ Fe_3O_4 (area 5), in which the P_{H_2O}/P_{H_2} requirement for $Fe_{0.947}O$ ↔ Fe_3O_4 is much higher than the previous step (Fe ↔ $Fe_{0.947}O$). As the temperature increases, the $Fe_{0.947}O$ → Fe_3O_4 transition become non-spontaneous, meaning higher P_{H_2O}/P_{H_2} or higher S_{steam} is needed to shift the equilibrium to the right.[48] However, area 2 shows inconsistent behaviour in the SR when T_{Fo} is between 450 °C and the disproportionation temperature (590 °C). S_{steam} slightly increases when T_{Fo} drops from 590 °C to 450 °C. Gleeson *et al.* stated that the $Fe_{0.947}O$ phase was thermodynamically stable beyond 590 °C, and the reduction shifts from Fe ↔ $Fe_{0.947}O$ ↔ Fe_3O_4 to Fe ↔ Fe_3O_4 below 590 °C.[49] Herein, the exothermic disproportionation reaction (eqn (9)) occurs below 590 °C. The released heat from the reaction (eqn (9)) results in an increase in temperature. At higher S_{steam}, less $Fe_{0.947}O$ is available for the disproportionation as $Fe_{0.947}O$ converts to Fe in the SR when M_{H_2} is higher. Thus, T_{Fo} has insignificant influences on the hydrogen generation (area 2 shrinks).

Effect of ammonia to OC ratio ($R_{NH_3/OC}$)

Fig. 6 shows the effect of $R_{NH_3/OC}$ on the performance of the CLCr process. In this study, the OC flow rate is 20 000 kg h^{-1} and the ammonia flow rates vary from 1000 to 1900 kg h^{-1} in order to achieve an ammonia to OC ratio ($R_{NH_3/OC}$) of 10.5–20. The AR outlet is fully oxidised at 960 °C under stoichiometric air flow conditions.

As can be seen from Fig. 6, the flow rate of the feed ammonia has an effect on the overall performance of the process. As $R_{NH_3/OC}$ increases, Y_{H_2} and E_{red} in FR increase. T_{Fo} and T_{So} drops continuously as the heat demand in the FR increases. As mentioned previously, $Fe_{0.947}O$ disproportionation occurs when T_{Fo} falls to 590 °C. Therefore, $X_{Fe_3O_4}$ and X_{Fe} increase significantly as the phase equilibria shifts from Fe_3O_4 ↔ $Fe_{0.947}O$ ↔ Fe to Fe_3O_4 ↔ Fe in the FR, while $X_{Fe_{0.947}O}$ significantly decreases. The exothermic reaction (eqn (9)) leads to a sudden rise in T_{Fo}. All the hydrogen from ammonia decomposition is consumed until T_{Fo} reaches 590 °C. When the disproportionation occurs, V_{H_2} increases with $R_{NH_3/OC}$. The reduction rate of Fe_3O_4 was found to be maximum at approximately 580 °C, when magnetite was used, and an E_{red} of 20–60% was applied.[50] Herein, the increase of V_{H_2} is due to the drop in reduction rates. This also explains the slower increase in E_{red} once T_{Fo} decreases to 590 °C. The disproportionation in the SR leads to a sudden increase in T_{So}, which aligns with the observations mentioned previous section, as S_{steam} increases below 590 °C. When T_{Ao} is at 960 °C and T_{Fo} is close to 590 °C, the value of $R_{NH_3/OC}$ should be ~14.5 to achieve the optimal E_{red} and hydrogen utilisation in the FR.

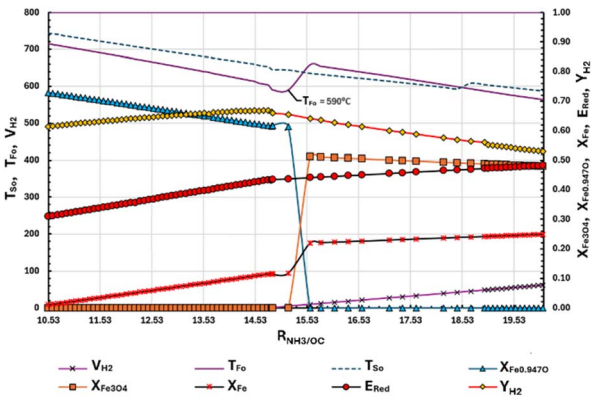

Fig. 6 Effect of $R_{NH_3/OC}$ on hydrogen yield (Y_{H2}), extent of reduction (E_{red}), mass fractions of Fe_3O_4, $Fe_{0.947}O$ and Fe in reduced oxides ($X_{Fe_3O_4}$, $X_{Fe_{0.947}O}$, X_{Fe}), unutilised H_2 in the FR vent (V_{H_2}), SR outlet temperature (T_{So}), and FR outlet temperature (T_{Fo}).

Effect of steam reactor pressure

The pressure has no effect on the hydrogen yield, as the gas ratios in the SR are equimolar.[51] However, high pressures in the SR can reduce the power of the compressor in the subsequent hydrogen compression stage. An SR pressure in the range of 1–15 bars was studied, and their performance was compared and summarised in Table 5 (calculations shown in SI).

The cold gas efficiency slightly decreases as the SR pressure increases, with a reduced conversion of $Fe_{0.947}O$. The temperature rise in the SR decreases, indicating a reduced heat of the reaction. As a result, the mass fraction of $Fe_{0.947}O$ increases with the pressure. The pressure shows a limited impact on the overall performance. Similar trends were reported in previous literature on syngas cracking in CL.[52] There is no correlation between pressure and hydrogen purity in the SR vent, which was validated by experiments, as hydrogen purities are beyond 99.99% at higher pressures.

Clearly, the power requirement of the subsequent hydrogen compression can be eliminated when the pressure is above 5 bar, as water condensation is improved by elevating the dew points. This also enhances the latent heat consumption, resulting in an increase in the overall energy efficiency.

Model optimisation

Determination of the optimal operating temperature ($\Delta_{Optimal}$). The objective of the model optimisation process is to determine the optimal operating temperature ($\Delta_{Optimal}$) for T_{Ao},

Table 5 Performance with SR pressure varying from 1 to 15 bars

Parameter	1 bar	5 bar	10 bar	15 bar
η_{CGE} (%)	74.19	74.13	74.03	73.95
η_{OEE} (%)	69.07	75.51	75.41	75.33
Hydrogen purity (%, mol mol^{-1})	99.91	>99.99	>99.99	>99.99
$W_{Fe_{0.947}O}$ (wt%)	12.5	12.6	12.7	12.9
ΔT_{SR} (°C $kmol^{-1}$–O_2)	1.314	1.294	1.267	1.24
W_{comp} (kWh)	307	0	0	0

Open Access Article. Published on 31 2025. Downloaded on 14.12.2025 04:25:05.
This article is licensed under a Creative Commons Attribution 3.0 Unported Licence.

under which an autothermal condition is achieved with the optimal value of the overall energy efficiency (η_{OEE}) and high hydrogen yield (Y_{H_2}). The simulations were carried out by varying the AR outlet temperature (T_{Ao}) and the ammonia to OC ratio ($R_{NH_3/OC}$). The $R_{NH_3/OC}$ was adjusted to achieve the highest E_{red} at each T_{Ao} (880–1050 °C).

A few assumptions were made: (1) the unutilised hydrogen (V_{H_2}) for the FR is negligible to maximise hydrogen yield; (2) the FR outlet temperature (T_{Fo}) was maintained to be close to 590 °C to exhibit stable phase equilibria; and (3) all reactions in the AR and the SR are stoichiometric.

As shown in Fig. 7, when T_{Ao} is around 900 °C and $R_{NH_3/OC}$ is 13.60, η_{OEE} reaches its maximum value (71.7%). When T_{Ao} is 880 or 890 °C, Y_{H_2} is equal to the theoretical maximum hydrogen yield ($Y_{H_2,\ max}$) but with a sacrifice of η_{OEE}. At T_{Ao} = 900 °C, Y_{H_2} starts to drop continuously due to the increase in E_{red}. In terms of the fraction of fuel energy lost as heat (F_L), the system exhibits a lower loss at T_{Ao} of 900 °C. Therefore, T_{Ao} of 900 °C was selected for the following process intensification.

Process intensification. The aim of process intensification is to further improve the overall energy efficiency (η_{OEE}) and the hydrogen yield (Y_{H_2}) through the extent of reduction (E_{red}), with a minimised loss of fuel energy as heat (F_L) for high-purity hydrogen production (with T_{Ao} = 900 °C). As described in the previous section, the energy demand of the compressor (W_{comp}) can be eliminated when the SR pressure is equal to 5 bar. On the other hand, the power requirement for pressurised water (W_{pump}) is 0.31 kWh. Therefore, η_{OEE} significantly increases while F_L reduces, achieving 78.2% and 17.8%, respectively. At this stage, the purity of hydrogen is above 99.99%. In an autothermal process, external energy consumption is zero. The temperature of preheated air can be reduced to 210 °C as the steam latent heat load decreases in the ammonia vaporiser. The key operating condition of the intensified process is presented in Fig. 8. Under the optimised conditions, the overall energy efficiency (η_{OEE}) reaches 79.6%, with a hydrogen yield (Y_{H_2}) of 69.4%.

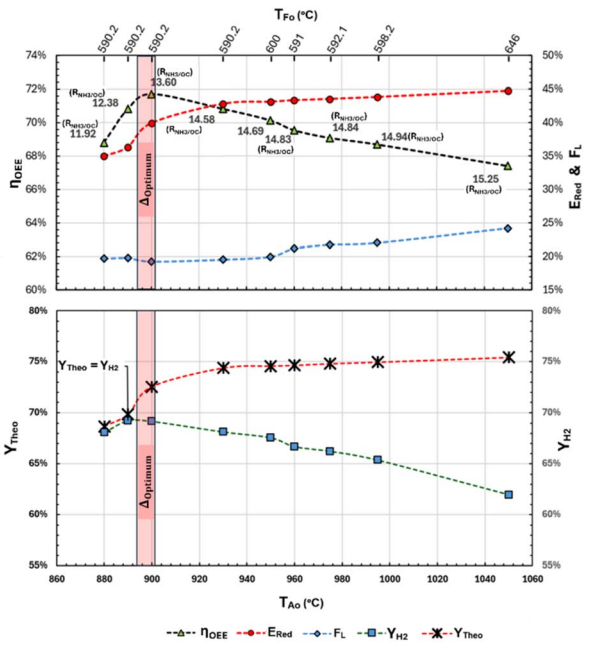

Fig. 7 Comparison of the extent of reduction (E_{red}), fractional ammonia fuel energy loss (F_L), overall energy efficiency (η_{OEE}), theoretical maximum H_2 yield (Y_{Theo}), and actual H_2 yield (Y_{H_2}) for T_{Ao} varying from 880–1050 °C and $R_{NH_3/OC}$ varying from 11.92 to 15.25.

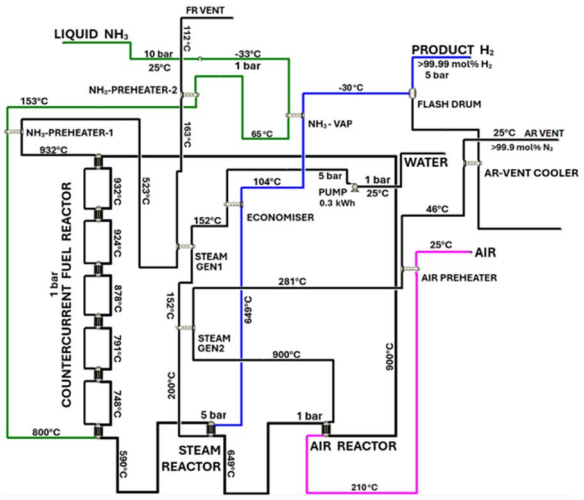

Fig. 8 Schematic diagram of the optimised model with key operating conditions.

Thermodynamic performance analysis of the optimised model

Heat balance. Table 6 presents the results from the heat calculations for the optimised model (Fig. 8). Details of the calculations can be found in Supplementary Information. As shown in Table 6, the net heat consumed is 9349.6 MJ h^{-1}, while the net heat generated is 9497.8 MJ h^{-1}, confirming that the CLCr process is autothermal.

Exergy analysis. The total exergy of the inlet and outlet streams (in MJ h^{-1}) was calculated using eqn (27) and (28), with the results summarised in Table 7. The total exergy of the inlet and outlet streams are 24 770.9 MJ h^{-1} and 19 400.5 MJ h^{-1}, respectively, with an overall exergy efficiency (η_e) of 70.4% (calculated using eqn (26)). Of the total unused exergy, about 71.6% was destroyed during the CLCr process (*e.g.*, high irreversibility of the reactions), and the other 28.4% was wasted in the exhaust streams (spent air and FR vent).[53] The exergy

Table 6 Net heat demands in the heat sink and heat sources in MJ h^{-1}

	In		Total
Heat sink	From FR inlet (feed oxides)	27 400	27 737.8
	From ammonia (feed ammonia)	337.8	
	Out		
	From FR outlet (reduced oxides)	11 073.1	18 388.2
	From process	7315.1	
	Heat sink balance (in–out)		9349.6
Heat sources	$\Delta H^0_{Comb_{NH_3\text{-fuel}}}$	8740.1	9497.8
	ΔH^0_{SR}	757.7	
	Heat sources balance		9497.8

This journal is © The Royal Society of Chemistry 2025

Open Access Article. Published on 31 2025. Downloaded on 14.12.2025 04:25:05. This article is licensed under a Creative Commons Attribution 3.0 Unported Licence.

Table 7 Exergy of the inlet and outlet streams

	Streams	Physical exergy	Chemical exergy	Total exergy
Inlet	Ammonia	392.4	24 170	24 562.4
	Air	−2.7	109.3	106.6
	Water	0	101.9	101.9
Outlet	Fuel reactor vent	813.5	957.2	1770.7
	SR vent	314.2	0	314.2
	Air reactor vent	−2.1	42.7	40.6
	Removed water	0	−0.4	−0.4
	Product hydrogen	0	17 275.4	17 275.4

destruction mainly arises from the irreversibility of the redox reactions of the Fe-based OC. The extent of irreversibility could be reduced by employing alternative OCs, or combining Fe-based OC with materials with narrower thermodynamic gaps between the reduction and oxidation steps, such as mixed oxides-based materials (*e.g.*, CeO_2).[54,55] Further exergy reduction could be achieved through enhanced heat recovery or advanced reactor design for better temperature control.

Techno-economic analysis. To evaluate the economic viability of the proposed system, a preliminary techno-economic analysis (TEA) was carried out to estimate the cost of the hydrogen produced from the process and identify key contributors to its cost. As a detailed TEA is not the main focus of this study, the calculation methodology, assumptions, and supporting data are provided in the Supplementary Information file.

The levelised cost of hydrogen (LCOH) estimated from the purchased equipment cost was \$4.61 kg^{-1} with the optimised case and the price of the feed ammonia being \$0.47 kg^{-1}.[56] The price of the feed ammonia was identified to be the largest contributor to the LCOH (84.4%), followed by annual capital expenditure (12.2%), variable operating capital (2.2%), and fixed operating capital (1.1%). The proposed process shows good potential in terms of economic viability, in line with findings from large-scale green ammonia decomposition studies reporting an LCOH of \$5.1 kg^{-1},[57] which can be further reduced to \$3.4 kg^{-1} with a cheaper ammonia cost of \$0.25 kg^{-1}.

Limitations and future work

Although there are existing studies on CL CH_4 cracking for hydrogen production,[58] CL NH_3 synthesis,[59] and syngas production with NH_3 and CO_2 through CL,[60] to the best of the authors' knowledge, this work is the first attempt to model and evaluate a CL system for hydrogen production through NH_3 cracking using Fe-based oxygen carriers. While the thermodynamic modelling in this study successfully demonstrated the potential of the proposed NH_3 CLCr process, several limitations of this work should be acknowledged. First, the simulations were carried out under equilibrium assumptions without explicit consideration of reaction kinetics or mass transfer limitations. Incorporating kinetic models into future simulations will better capture the iron oxide redox cycles and NH_3 conversion, especially at lower operating conditions. Second, some practical material and operational challenges still remain. The long-term durability of iron oxides under repeated cycling may be impaired due to sintering and potential formation of iron nitride species.[61] Experimental studies of iron oxides under an NH_3 environment is needed as part of the future work to provide useful information on the stability of the Fe-based OCs. Finally, the development of OCs with smaller irreversibility of the redox reactions, and better heat integration are needed.[62]

Conclusions

In this study, a novel ammonia cracking chemical looping process for high-purity hydrogen production was designed and evaluated through process modelling and thermodynamic analysis. Iron oxide was selected as the oxygen carrier. A parametric study was carried out to evaluate the effect of key operating conditions on the process performance. The results demonstrated that an AR outlet temperature of 960 °C, an FR outlet temperature of 590 °C, and an ammonia to OC carrier ratio of 14.5 provided optimal conditions for maximising hydrogen yield and energy efficiency, while minimising process energy losses. Process intensification strategies, such as increasing the SR pressure to 5 bar, can help achieve an overall energy efficiency of 78%, exergy efficiency of 70.9%, and a hydrogen yield of 69.4% with a purity above 99.99%. Under steady operation, the process is autothermal, without the requirement of external heating. These findings highlight the potential of the CLCr process as a scalable and energy-efficient method for producing high-purity hydrogen from ammonia. This study paves the way for further experimental validation to assess the reaction kinetics and oxygen carrier stability, as well as techno-economic analysis to evaluate its feasibility for industrial-scale implementation.

Author contributions

Anantha Krishnan Vinayak Soman: formal analysis, data curation, writing – original draft. Siqi Wang: formal analysis, data curation, writing – original draft. Ziqi Shen: formal analysis, writing – original draft. Mingming Zhu: funding acquisition, conceptualisation, supervision, writing – review & editing.

Conflicts of interest

There are no conflicts to declare.

Open Access Article. Published on 31 2025. Downloaded on 14.12.2025 04:25:05. This article is licensed under a Creative Commons Attribution 3.0 Unported Licence.

Data availability

The data supporting this article have been included as part of the supplementary information (SI). Supplementary information: detailed calculation of heat balance and techno-economic analysis. See DOI: **https://doi.org/10.1039/d5se01010a**.

Acknowledgements

This work was supported by grants from Engineering and Physical Sciences Research Council, UK (EP/X03593X/1).

References

1 S. A. Ansari, M. W. Alam, N. Dhanda, M. S. Abbasi, M. E. Ahmed, A. bader alrashidi, A. M. Al-Farhan and B. Abebe, *Global Challenges*, 2025, **9**(6), DOI: **10.1002/gch2.202500086**.
2 C. H. Christensen, T. Johannessen, R. Z. Sørensen and J. K. Nørskov, *Catal. Today*, 2006, **111**, 140–144.
3 Y. Kojima, *Int. J. Hydrogen Energy*, 2019, **44**, 18179–18192.
4 E. Spatolisano and F. Restelli, *Chem. Eng. Trans.*, 2024, **109**, 2024.
5 J. Ashcroft and H. Goddin, *Johnson Matthey Technol. Rev.*, 2022, **66**, 375–385.
6 Z. P. Hu, C. C. Weng, C. Chen and Z. Y. Yuan, *Appl. Catal., A*, 2018, **562**, 49–57.
7 C. Zhou, K. Wu, H. Huang, C. F. Cao, Y. Luo, C. Q. Chen, L. Lin, C. Au and L. Jiang, *ACS Catal.*, 2021, **11**, 10345–10350.
8 R. Campo, P. Durán, J. Plou, J. Herguido and J. A. Peña, *J. Power Sources*, 2013, **242**, 520–526.
9 S. Sun, M. Zhao, L. Cai, S. Zhang, D. Zeng and R. Xiao, *Energy Fuels*, 2015, **29**, 7612–7621.
10 J. Plou, P. Durán, J. Herguido and J. A. Peña, *Int. J. Hydrogen Energy*, 2016, **41**, 19349–19356.
11 Q. Imtiaz, N. S. Yüzbasi, P. M. Abdala, A. M. Kierzkowska, W. Van Beek, M. Broda and C. R. Müller, *J. Mater. Chem. A*, 2015, **4**, 113–123.
12 Y. D. Wang, X. N. Hua, C. C. Zhao, T. T. Fu, W. Li and W. Wang, *Int. J. Hydrogen Energy*, 2017, **42**, 5667–5675.
13 M. Saeedan and E. Houshfar, *Fuel Process. Technol.*, 2025, **273**, 108230.
14 M. Mohammadpour, A. Mohammadpour, M. Ashjaee and E. Houshfar, *J. CO_2 Util.*, 2025, **93**, 103044.
15 M. Luo, Y. Yi, S. Wang, Z. Wang, M. Du, J. Pan and Q. Wang, *Renewable Sustainable Energy Rev.*, 2018, **81**, 3186–3214.
16 E. Karimi, H. R. Forutan, M. Saidi, M. R. Rahimpour and A. Shariati, *Energy Fuels*, 2014, **28**, 2811–2820.
17 H. R. Forutan, E. Karimi, A. Hafizi, M. R. Rahimpour and P. Keshavarz, *J. Ind. Eng. Chem.*, 2015, **21**, 900–911.
18 T. Triana, G. A. Brooks, M. A. Rhamdhani and M. I. Pownceby, *J. Sustain. Metall.*, 2024, **10**, 1428–1445.
19 I. Iwamoto, A. Kurniawan, H. Hasegawa, Y. Kashiwaya, T. Nomura and T. Akiyama, *ISIJ Int.*, 2022, **62**, 2483–2490.
20 Y. Ma, J. W. Bae, S. H. Kim, M. Jovičević-Klug, K. Li, D. Vogel, D. Ponge, M. Rohwerder, B. Gault and D. Raabe, *Adv. Sci.*, 2023, **10**, 2300111.
21 I. Lucentini, X. Garcia, X. Vendrell and J. Llorca, *Ind. Eng. Chem. Res.*, 2021, **60**, 18560–18611.
22 F. Kong, C. Li, Y. Zhang, Y. Gu, M. Kathe, L. S. Fan and A. Tong, *Energy Technol.*, 2020, **8**, 1900377.
23 G. T. Furukawa, T. B. Douglas, R. E. Mccoskey and D. C. Ginnings, *J. Res. Natl. Bur. Stand. (U. S.)*, 1956, **57**(2), RP2694.
24 N. S. Yüzbasi, A. Kierzkowska and C. Müller, *Energy Procedia*, 2017, **114**, 436–445.
25 W. X. Meng, S. Banerjee, X. Zhang and R. K. Agarwal, *Energy*, 2015, **90**, 1869–1877.
26 R. Porrazzo, G. White and R. Ocone, *Fuel*, 2014, **136**, 46–56.
27 D. Sridhar, A. Tong, H. Kim, L. Zeng, F. Li and L. S. Fan, *Energy Fuels*, 2012, **26**, 2292–2302.
28 L. Zeng, F. He, F. Li and L. S. Fan, *Energy Fuels*, 2012, **26**, 3680–3690.
29 R. Joshi, Y. Pottimurthy, V. Shah, P. Mohapatra, S. Kumar, O. Jones, M. Beard, I. Harry, A. Hornbuckle, M. Kathe and L. S. Fan, *Ind. Eng. Chem. Res.*, 2021, **60**, 11231–11240.
30 S. Mukherjee, P. Kumar, A. Yang and P. Fennell, *J. Environ. Chem. Eng.*, 2015, **3**, 2104–2114.
31 Q. Zhang, R. K. Joshi, D. Xu, A. Tong and L. S. Fan, *Int. J. Hydrogen Energy*, 2024, **49**, 823–839.
32 A. Yerrayya and P. V. Suresh, *J. Ind. Pollut. Control*, 2021, **6**, 390–396.
33 W. X. Meng, S. Banerjee, X. Zhang and R. K. Agarwal, *Energy*, 2015, **90**, 1869–1877.
34 N. Khallaghi, D. P. Hanak and V. Manovic, *Appl. Energy*, 2019, **249**, 237–244.
35 L. Liu, H. Cao, D. Xiang, Y. Xia, P. Li and Z. Zhou, *J. Cleaner Prod.*, 2023, **417**, 137960.
36 Ö. Ç. Mutlu and T. Zeng, *Chem. Eng. Technol.*, 2020, **43**, 1674–1689.
37 S. Begum, M. G. Rasul, D. Akbar and N. Ramzan, *Energies*, 2013, **6**, 6508–6524.
38 M. Jasper, A. Shahbazi, · Keith Schimmel, F. Li and L. Wang, *Discover Chem. Eng.*, 2023, **3**(1), 1–22.
39 V. H. Collins-Martinez, J. F. Cazares-Marroquin, J. M. Salinas-Gutierrez, J. C. Pantoja-Espinoza, A. Lopez-Ortiz and M. J. Melendez-Zaragoza, *RSC Adv.*, 2020, **11**, 684–699.
40 D. P. Hanak, B. G. Jenkins, T. Kruger and V. Manovic, *Appl. Energy*, 2017, **205**, 1189–1201.
41 M. Rokni, *Introduction to Pinch Technology Division of Energy Section Introduction to Pinch Technology*, 2006.
42 L. Santini, C. Accornero and A. Cioncolini, *Appl. Energy*, 2016, **181**, 446–463.
43 National Energy Technology Laboratory, *Quality Guidelines for Energy System Studies Process Modeling Design Parameters*, 2019.
44 International PtX Hub, *Ammonia Transport & Storage*, 2024.
45 D. Spreitzer and J. Schenk, *Steel Res. Int.*, 2019, **90**, 1900108.
46 C. D. Bohn, C. R. Müller, J. P. Cleeton, A. N. Hayhurst, J. F. Davidson, S. A. Scott and J. S. Dennis, *Ind. Eng. Chem. Res.*, 2008, **47**, 7623–7630.
47 A. Pineau, N. Kanari and I. Gaballah, *Thermochim. Acta*, 2006, **447**, 89–100.

 This journal is © The Royal Society of Chemistry 2025

Open Access Article. Published on 31 2025. Downloaded on 14.12.2025 04:25:05.
This article is licensed under a Creative Commons Attribution 3.0 Unported Licence.

48 K. Svoboda, G. Slowinski, J. Rogut and D. Baxter, *Energy Convers. Manage.*, 2007, **48**, 3063–3073.
49 B. Gleeson, S. M. M. Hadavi and D. J. Young, *Mater. High Temp.*, 2000, **17**, 311–318.
50 A. Pineau, N. Kanari and I. Gaballah, *Thermochim. Acta*, 2007, **456**, 75–88.
51 M. Bleeker, S. Gorter, S. Kersten, L. Van Der Ham, H. Van Den Berg and H. Veringa, *Clean Technol. Environ. Policy*, 2010, **12**, 125–135.
52 G. Voitic, S. Nestl, K. Malli, J. Wagner, B. Bitschnau, F. A. Mautner and V. Hacker, *RSC Adv.*, 2016, **6**, 53533–53541.
53 A. P. Simpson and A. E. Lutz, *Int. J. Hydrogen Energy*, 2007, **32**, 4811–4820.
54 A. Hedayati, A. M. Azad, M. Rydén, H. Leion and T. Mattisson, *Ind. Eng. Chem. Res.*, 2012, **51**, 12796–12806.
55 L. Brinkman, B. Bulfin and A. Steinfeld, *Energy Fuels*, 2021, **35**, 18756–18767.
56 L. Hatton, R. Bañares-Alcántara, S. Sparrow, F. Lott and N. Salmon, *Int. J. Hydrogen Energy*, 2024, **49**, 635–643.
57 C. Makhloufi and N. Kezibri, *Int. J. Hydrogen Energy*, 2021, **46**, 34777–34787.
58 J. Hu, V. V. Galvita, H. Poelman and G. B. Marin, *Materials*, 2018, **11**, 1187.
59 B. Wang and L. Shen, *Ind. Eng. Chem. Res.*, 2022, **61**, 18215–18231.
60 M. Keller and A. Sharma, *J. CO2 Util.*, 2023, **76**, 102588.
61 T. Triana, G. A. Brooks, M. A. Rhamdhani and M. I. Pownceby, *J. Sustain. Metall.*, 2024, **10**, 1428–1445.
62 A. Coppola and F. Scala, *Energy Fuels*, 2021, **35**, 19248–19265.